Translational Oncology 57 (2025) 102393

Contents lists available at ScienceDirect

Translational Oncology

journal homepage: www.elsevier.com/locate/tranon

Original Research

Carfilzomib promotes Iodine-125 seed radiation-induced apoptosis, paraptosis, and ferroptosis in esophageal squamous cell carcinoma by aggravating endoplasmic reticulum stress

Chao Wang [a], Yin-Lin Zha [b], Hao Wang [a], Bai Sun [a], Wei-Guang Qiang [a], Ye Yuan [a], Hong-Bing Shi [a,*], Wen-Wei Hu [a,c,*]

[a] Department of Oncology, The Third Affiliated Hospital of Soochow University, Changzhou, 213003, Jiangsu, PR China
[b] Department of Radiation Oncology, the Third Affiliated Hospital of Soochow University, Changzhou, 213003, Jiangsu, PR China
[c] Jiangsu Engineering Research Center for Tumor Immunotherapy, The Third Affiliated Hospital of Soochow University, Changzhou, 213003, Jiangsu, PR China

ARTICLE INFO

Keywords:
Iodine-125
Carfilzomib
Apoptosis
Ferroptosis
Esophageal cancer

ABSTRACT

Iodine-125 (^{125}I) seed brachytherapy has been applied to treat various malignant tumors such as esophageal cancer, however, radioresistance can reduce its efficacy. Endoplasmic reticulum stress (ERS) and subsequent unfolded protein response (UPR) is one of the core mechanisms of ^{125}I seed radiation-induced cell death, thus aggravating ERS has been considered a promising sensitization strategy. Herein, we show that combination therapy of an irreversible proteasome inhibitor carfilzomib (CFZ) and ^{125}I seed radiation displayed strong anti-tumor effect on esophageal squamous cell carcinoma (ESCC). Mechanistically, ERS and UPR regulated multiple cell death modalities induced by the combination therapy, including apoptosis, paraptosis, and ferroptosis. ^{125}I seed radiation induced reactive oxygen species (ROS) production, DNA damage, p53 activation, and apoptosis. CFZ promoted ROS production, and augmented ^{125}I seed radiation-induced apoptosis via the mitochondrial pathway, which was mediated by the UPR-C/EBP homologous protein (CHOP) pathway and was independent of the p53 pathway. CFZ enhanced ^{125}I seed radiation-induced intracellular Ca^{2+} overload, protein ubiquitination, ERS, and UPR, consequently promoting paraptosis. ^{125}I seed radiation induced accumulation of intracellular Fe^{2+} and lipid peroxides but upregulated the expression of ferroptosis inhibitors, SLC7A11 and glutathione peroxidase 4 (GPX4). The combination therapy promoted ferroptosis by enhancing the accumulation of intracellular Fe^{2+} and downregulating GPX4 expression. The mouse experiment demonstrated that CFZ can promote the efficacy of ^{125}I seed radiation with good tolerance. Our findings suggest that combination therapy of ^{125}I seed radiation and CFZ is associated with multiple cell death modalities and may serve as a promising therapeutic strategy for ESCC.

Introduction

Globally, esophageal cancer is the seventh most common cancer [1]. Esophageal squamous cell carcinoma (ESCC) accounts for approximately 90 % of esophageal cancer cases, and most patients with ESCC are initially diagnosed with locally advanced or metastatic disease [2]. Systemic therapies, including chemotherapy, immunotherapy, and radiation therapy, are used to control tumors, improve the success rate of surgery, and prolong patients' survival [3]. As a type of radiation therapy, iodine-125 (^{125}I) seed continuous low-dose-rate (CLDR) brachytherapy has been applied to treat various malignant tumors, such as advanced esophageal cancer [4]. ^{125}I seed brachytherapy is currently used clinically as a salvage therapy for lymph node metastasis and a palliative treatment for malignant dysphagia in the current clinic. ^{125}I seed implantation can effectively control lymph node recurrence secondary to esophageal cancer [5,6], and ^{125}I seed-loaded stent placement can relieve malignant dysphagia and improve survival [7]. Unfortunately, ^{125}I seed brachytherapy causes tumor radioresistance like other types of radiation therapy and lacks effective radiosensitizers.

The endoplasmic reticulum (ER) is responsible for protein synthesis, folding, and transport. Accumulation of unfolded and misfolded proteins in the ER lumen causes ER stress (ERS) and activates the unfolded protein response (UPR) to maintain ER homeostasis. The UPR performs functions through three canonical pathways: PERK-eIF2α-ATF4, IRE-1-

* Corresponding authors.
E-mail addresses: shbcyr@163.com (H.-B. Shi), viphuwenwei@vip.163.com (W.-W. Hu).

https://doi.org/10.1016/j.tranon.2025.102393
Received 3 September 2024; Received in revised form 9 February 2025; Accepted 7 April 2025

XBP1, and ATF6. During persistent ERS, three UPR pathways upregulate the expression of transcription factor C/EBP homologous protein (CHOP). CHOP plays a dual role in cell death; it not only activates the mitochondrial apoptosis pathway but also participates in the formation of autophagosomes [8]. On the other hand, persistent high ERS can cause ER swelling and vacuolization, ultimately triggering paraptosis, a non-canonical cell death characterized by a network of vacuoles that gradually fills the entire cytoplasmic space [9,10].

Previous studies have demonstrated that apoptosis is the primary modality of cell death induced by ^{125}I seed radiation, and ERS is one of the core mechanisms of ^{125}I seed radiation-induced apoptosis [11,12]. Therefore, aggravating ERS is expected to be an effective sensitization strategy. However, during ERS, cells also initiate ER-associated degradation (ERAD) to degrade unfolded and misfolded proteins, thereby maintaining cellular proteostasis and inhibiting cell death. The ubiquitin-proteasome system severs a dominant role in ERAD. Small-molecule inhibitors targeting ubiquitin-proteasome system have demonstrated radiosensitization effects in various cancers [13]. For example, the proteasome inhibitor marizomib promotes the sensitivity of medulloblastoma cells to γ-irradiation by enhancing ROS generation, stabilizing p53, and activating caspases, thereby leading to apoptosis [14] As an irreversible proteasome inhibitor targeting the 20S proteasome core, carfilzomib (CFZ) can inhibit the degradation of unfolded and misfolded proteins, thus aggravating ERS and enhancing apoptosis [15]. CFZ has been approved for treating multiple myeloma and may have a good extension of clinical application [16].

In this study, we evaluated the sensitizing effect of CFZ on ^{125}I seed radiation in ESCC cells and explored the mechanism by which combination therapy induces cell death. Interestingly, the combination therapy of ^{125}I seed radiation and CFZ induced not only apoptosis and paraptosis but also ferroptosis. Mechanistic studies revealed that ERS and UPR dominated the regulation of cell death modalities. CFZ aggravated ^{125}I seed radiation-induced ERS, further inducing UPR-CHOP-mediated mitochondrial apoptosis and ERS-related paraptosis. The combination therapy induced ferroptosis through multiple mechanisms, such as enhanced accumulation of intracellular Fe^{2+}, potentially regulated by ERS, and downregulation of glutathione peroxidase 4 (GPX4) expression. Our findings demonstrate that combination therapy can induce multiple modalities of cell death by aggravating ERS, and provide a promising sensitization strategy for ^{125}I seed brachytherapy of ESCC.

Materials and methods

Cell culture and siRNA transfection

Human ESCC cell line Kyse-150 was obtained from the Cell Bank of Type Culture Collection of Chinese Academy of Sciences (Shanghai, China), and EC-109 was purchased from Cellcook Biotech (Guangzhou, China). Cell line authentication was performed using STR profiling. The cells were cultured at 37 °C with 5 % CO_2 in RPMI 1640 medium (#11,875, Gibco, Thermo Fisher Scientific, Waltham, MA, USA), supplemented with 10 % fetal bovine serum (#10,099, Gibco) and 1 % penicillin/streptomycin (#15,140, Gibco).

CHOP-specific siRNA (sequences: 5'-GCCTGGTATGAGGACCTGC-3') and the non-specific control were purchased from RiboBio Technology (Guangzhou, China). Cells were seeded into 6-well plates in antibiotic-free media and transfected at with 50 nM siRNA in Opti-MEM (#31,985, Invitrogene, Thermo Fisher Scientific) using Lipofectamine 2000 (#11,668, Invitrogene) according to the manufacturer's instructions. To confirm successful siRNA-mediated knockdown, Western blot analysis of CHOP protein was performed. Cells were applied to further treatment 24 h after transfection.

Chemicals, reagents, and antibodies

Carfilzomib (CFZ; #A1933), ferrostatin-1 (Fer-1; #A4371), deferoxamine (DFO; #B6068), and cell counting kit-8 (CCK-8, #K1018) were purchased from APExBIO Technology (Houston, TX, USA). Cycloheximide (CHX; #HY-12,320) was purchased from Medchem Express (Monmouth Junction, NJ, USA). Annexin V-FITC apoptosis detection kit (#C1062), 5-ethynyl-2′-deoxyuridine (EdU) cell proliferation kit (#C0075), dimethyl sulphoxide (DMSO; #ST2335), 2′,7′-dichlorodihydrofluorescein diacetate (DCFH-DA; #S0033), and Fluo-3 AM (#S1056) were purchased from Beyotime Biotechnology (Shanghai, China). Rhod-2 AM (#40776ES) was purchased from Yeasen Biotechnology (Shanghai, China). FerroOrange (#F374) and Liperfluo (#L248) were purchased from Dojindo Laboratories (Kumamoto, Japan). Antibodies against p-H2AX (#9718), PARP (#9532), p53 (#2524), p-p53 (#9284), ubiquitin (Ub, #3936), p-eIF2α (#3398), IRE1α (#3294), ATF6 (#65,880), Alix (#92,880), LC3B (#3868), β-tubulin (#2128), β-actin (#4970) were purchased from Cell Signaling Technology (Danvers, MA, USA). Antibodies against caspase 3 (#19,677–1-AP), caspase 8 (#13,423–1-AP), caspase 9 (#10,380–1-AP), Grp78/Bip (#11,587–1-AP), CHOP (#15,204–1-AP), SLC7A11 (#26,864–1-AP), GPX4 (#67,763–1-Ig), heme oxygenase 1 (HO-1, #10,701–1-AP), and GAPDH (60,004–1-Ig) were purchased from Proteintech (Wuhan, China). SLC39A14 antibody (#DF14224) was purchased from Affinity Biosciences (Changzhou, China). 4-HNE antibody (#ab46545) was purchased from Abcam (Cambridge, UK). Horseradish peroxidase-conjugated goat anti-rabbit (#7074) and horse anti-mouse (#7076) IgG antibodies were purchased from Cell Signaling Technology.

Radiation source and irradiation procedure

^{125}I radioactive seeds (0.8 mCi, mode 6711) were provided by Larvin Bioengineering Technology Company (Shenzhen, China). The half-life of each ^{125}I seed is 59.4 days, and the principal photon emissions are 27.4–31.4 keV X-rays and 35.5 keV γ-rays. The *in-vitro* irradiation model was built according to the previous studies and was able to provide relatively homogeneous dose distribution [11,17]. This model consisted of a lower source plane and an upper cell plane, with a spacing of 6 mm. In the source plane, sixteen seeds were equidistantly spaced around a 35-mm diameter circumference, and two seeds were confined to the center. In the cell plane, cells were cultured in a 35-mm polystyrene dish, which overlapped with the circumference in the source plane (Fig. 1A). The initial dose rate in the cell plane was 5.55 cGy/h. The exposure time for delivering the cumulative radiation dose of 3 and 6 Gy were 55 and 112 h. The treatment planning system for ^{125}I seed brachytherapy (Larvin Bioengineering Technology Company) was used to verify the radiation dose. In the control group, the *in-vitro* irradiation model was made with sham seeds (0 mCi). According to the previous study, ESCC cells underwent obvious morphological changes and apoptosis at 6 Gy [11], so we took 6 Gy as the research dose. Intervening chemicals or reagents were added to the cells 24 h before the end of each irradiation.

Cell viability assay

Cells were seeded in 96-well plates (5×10^3–1×10^4 cells/well), cultured for 24 h, and then treated with CFZ (dissolved in 0.1 % DMSO) at concentrations ranging from 0 to 200 nM for 24 h, 48 h, or 72 h. The cells were incubated for an additional 1 h at 37 °C with 20 μl of CCK-8 solution in 200 μl culture medium, and the absorbance at 450 nm was measured by a microplate reader (Thermo Fisher Scientific). Cell viability in the control group (0.1 % DMSO treatment) was set to 100 %.

EdU staining assay

After the indicated treatments, cells were incubated with 10 μM EdU

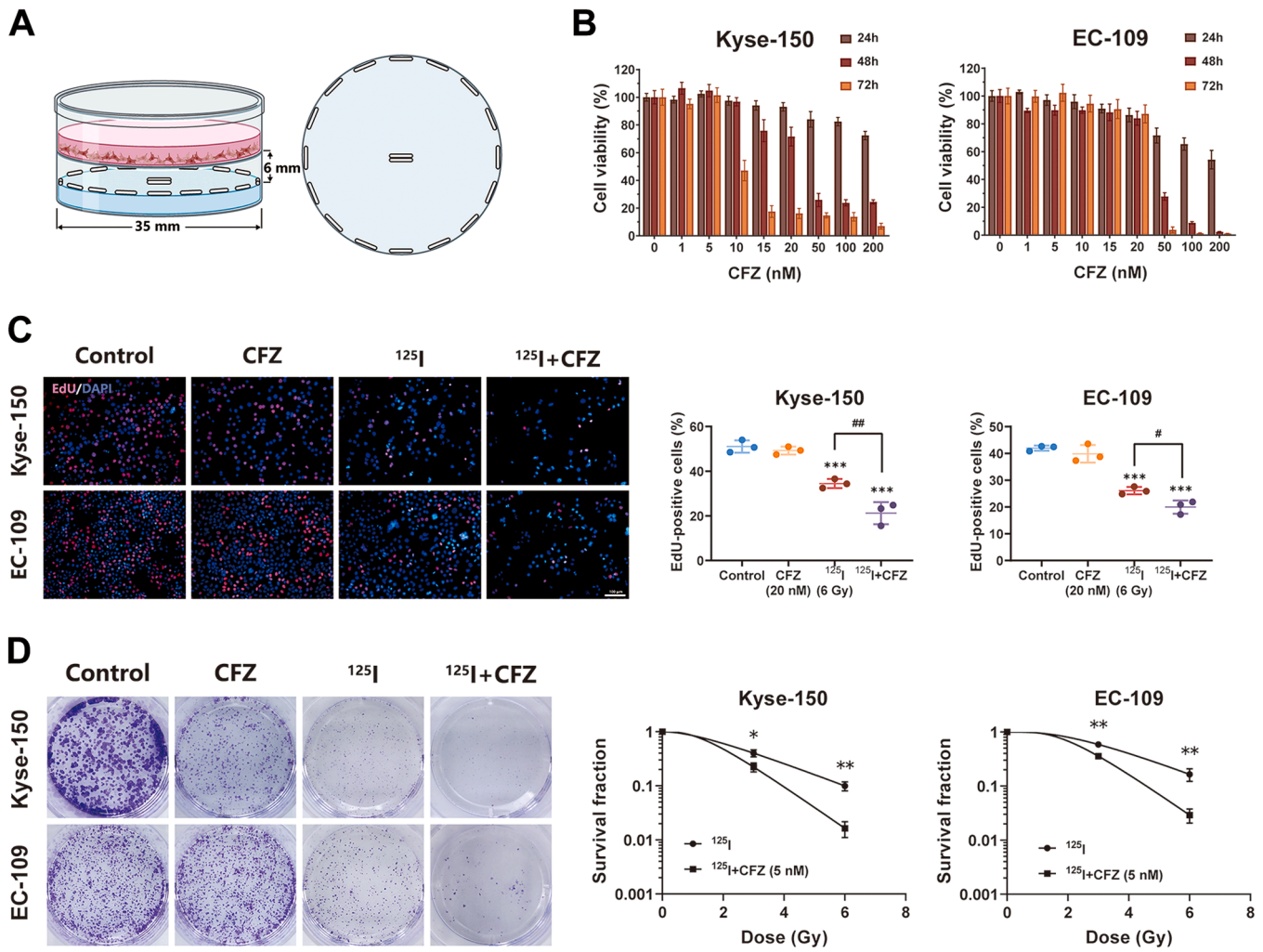

Fig. 1. CFZ promotes the radiosensitivity of ESCC cells to ^{125}I seed radiation. (A) Schematic illustration of the *in-vitro* irradiation model. (B) The toxicity analysis of CFZ to Kyse-150 and EC-109 cells. Cells were treated with CFZ at various concentrations (0–200 nM) for 24 h, 48 h, and 72 h, and the cell viability was measured using CCK-8 assay. (C) CFZ promoted the anti-proliferative effect of ^{125}I seed radiation in Kyse-150 and EC-109 cells. Cells were treated with ^{125}I seed radiation (6 Gy) and CFZ (20 nM, 24 h) alone or in combination, then stained with EdU and DAPI and observed under the fluorescence microscope. Scale bar = 100 μm. The percentage of EdU-positive cells was analyzed. (D) Radiosensitizing effect of CFZ on Kyse-150 and EC-109 cells. Cells were pretreated with 0.1 % DMSO or CFZ (5 nM) for 24 h, then seeded into the 35-mm culture dish and exposed to ^{125}I seed radiation (0, 3, or 6 Gy). After the treatment, cells were cultured in fresh medium for 7–9 days to form colonies. Survival fraction was calculated by colony formation assay. The dose-survival curves were fitted by the multi-target single-hit model. $N = 3$, $^{*}P < 0.05$, $^{**}P < 0.01$, and $^{***}P < 0.001$ compared to control group. $^{\#}P < 0.05$ and $^{\#\#}P < 0.01$ compared between indicated groups.

solution for 2 h at 37 °C. Then, cells were fixed with 4 % paraformaldehyde, washed, and permeabilized with 0.3 % Triton X-100. Next, EdU was labeled by Alexa Fluor 555 through the click reaction, and nuclei were stained with Hoechst 33,342. The cells were washed with phosphate buffer saline (PBS) and observed under the fluorescence microscope (Nikon, Tokyo, Japan).

Colony formation assay

After being treated with 0.1 % DMSO or 5 nM CFZ for 24 h, cells were collected as single-cell suspensions and seeded into the 35-mm culture dish at 1×10^3 cells/well. Subsequently, cells were placed in the irradiation model and underwent 0, 3, or 6 Gy irradiation and kept culturing without radiation for another 7–9 days to form colonies. The colonies were fixed with 4 % paraformaldehyde and then stained with 0.1 % crystal violet solution. The planting efficiency (PE) was defined as the ratio of colony number to inoculating cell number, and the survival fraction (SF) was defined as the ratio of PE (irradiated group) to PE (control group). The cell survival curve was fitted by the multi-target single-hit model: $SF = 1 - (1 - e^{-D/D0})^N$.

Annexin V-FITC-propidium iodide (PI) assay

Annexin V-FITC-PI staining was performed according to the manufacturer's instructions. After the indicated treatments, cells were harvested and washed with PBS. Then, cells were resuspended in 195 μl binding buffer, and incubated with 5μl Annexin V-FITC solution and 10 μl PI solution for 20 min at room temperature. For the PI assay, cells were incubated with PI solution only after being suspended in the binding buffer. The sample data was collected by flow cytometry (FCM; FACS Canto II, BD Biosciences, NJ, USA) within 1 h, and analyzed using FlowJo v 10.8.1 software (BD Biosciences).

Measurement of reactive oxygen species (ROS) and lipid peroxide

DCFH-DA was used to detect the intracellular ROS levels according to the manufacturer's protocol. After the indicated treatments, cells were incubated with 10 μM DCFH-DA for 30 min at 37 °C. Subsequently, the cells were washed with PBS, and collected as single-cell suspensions. The fluorescence intensity of DCF was measured through FCM and analyzed using FlowJo software.

Total cellular lipid peroxide was measured using the Liperfluo probe. After the indicated treatments, cells were washed with RPMI 1640 medium and then incubated with 5 μM Liperfluo solution for 30 min at 37 °C in serum-free medium. Labeled cells were washed with Hank's buffered salt solution (HBSS) to remove the excess Liperfluo probe. Then, cells were trypsinized, washed, and resuspended in HBSS for FCM analysis.

Measurement of intracellular free Ca^{2+} and Fe^{2+} levels

To measure cytosolic Ca^{2+} levels, cells were washed with HBSS (without Ca^{2+} or Mg^{2+}) and incubated with 2 μM Fluo-3 AM for 30 min at 37 °C after the indicated treatments. To measure mitochondrial Ca^{2+} levels, cells were washed with HBSS and incubated with 4 μM Rhod-2 AM for 30 min at 37 °C. Excess Fluo-3 AM or Rhod-2 AM was removed by washing labeled cells with HBSS. Cells were further incubated in HBSS for 20 min at 37 °C and then resuspended in HBSS for FCM analysis.

Intracellular Fe^{2+} levels were measured using the FerroOrange probe according to the manufacturer's protocol. After the indicated treatments, cells were trypsinized and washed with HBSS. Then, cells were resuspended in 300 μl serum-free medium and incubated with 1 μM FerroOrange solution for 30 min at 37 °C. Samples were analyzed through FCM within 1h .

Western blot analysis

Cells were lysed according to the protocol of a whole cell lysis assay kit (#KGP2100, Keygen Biotech, Nanjing, China). Cells were washed and lysed for 30 min in the ice-cold lysis buffer containing protease and phosphatase inhibitors. Cell lysates were centrifuged at 12,000 g and 4 °C for 15 min, after which protein supernatant concentrations were determined using the bicinchoninic acid method. The Western blot assay was performed according to the routine techniques. Samples (30 μg protein) were separated by Bis-Tris gel electrophoresis in MOPS running buffer. Proteins were transferred onto the PVDF membrane. The membranes were sequentially blocked with 5 % bovine serum albumin, incubated with primary antibodies, and then incubated with horseradish peroxidase-conjugated secondary antibodies. The ECL reagent and light capture system (Tanon, Shanghai, China) were used for detecting target bands. Optical densities of protein bands were analyzed using ImageJ v 1.51 software (National Institute of Health, MD, USA).

RNA isolation and transcriptome sequencing

After the indicated treatments, cells were washed with ice-cold PBS, and total RNA was extracted using the TRIzol reagent (Invitrogen) according to the manufacturer's protocol. RNA purity and quantification were evaluated using the NanoDrop 2000 spectrophotometer (Thermo Scientific). RNA integrity was assessed using the Agilent 2100 Bioanalyzer (Agilent Technologies, Santa Clara, *CA*, USA) and all RNA samples had a RIN >9.5.

The transcriptome libraries construction, sequencing, and analysis were conducted by OE Biotech Co., Ltd. (Shanghai, China). All libraries were sequenced on an Illumina Novaseq 6000 platform and ~50 M reads were generated (Pair-end 150 bp). Raw sequencing data was deposited in the SRA database, under BioProject number PRJNA1111689. Raw reads were processed using fastp software to remove low-quality reads, after which clean reads were retained for subsequent analyses. The clean reads were mapped to the human genome using HISAT2 software. FPKM values of each gene were calculated and the read counts of each gene were obtained by HTSeq-count software.

Differential expression analysis was performed using the DESeq2 software. Q value <0.05 and foldchange >2 or foldchange <0.5 was set as the threshold for significantly differentially expressed genes (DEGs). Hierarchical cluster analysis of DEGs was performed using R v 3.2.0 software. A volcano plot of DEGs was drawn using R packet ggplot2 to show the expression of upregulated or downregulated DEGs. Based on the hypergeometric distribution, GO functional enrichment analysis and KEGG pathway enrichment analysis of DEGs were performed to screen the significantly enriched terms and pathways using R software.

Animal models and treatments

Female BALB/c nude mice aged 4–6 weeks were purchased from Cavens Laboratory Animal Co., Ltd (Changzhou, China). Kyse-150 cells (5×10^6 in 0.1 ml PBS) were subcutaneously injected into the left axilla of nude mice using standard procedure. When the tumors grew to approximately 200 mm^3 in 10 days, the mice were randomly divided into four groups ($n = 5$/group). Grouping and treatments were as follows: (a) control group, mice received sham seed implantation and were treated with vehicle solution; (b) CFZ group, mice received sham seed implantation and were treated with CFZ; (c) ^{125}I group, mice received ^{125}I seed implantation and were treated with vehicle solution; (d) combined treatment group, mice received ^{125}I seed implantation and were treated with CFZ. Seed implantation was performed using an 18-gauge coaxial puncture needle, and an ^{125}I seed (1.0 mCi) or sham seed (0 mCi) was implanted into the center of each tumor. CFZ was dissolved in the vehicle solution (1 %DMSO, 30 % PEG300, and 2 % Tween 80 in ddH_2O) and given intraperitoneal at 0.425 mg/kg, for 3 consecutive days followed by a 4-day rest period. The control group received vehicle solution treatment using the same schedule. After seed implantation, tumor volumes and body weight were measured every 3 days. Tumor volume was calculated using the following formula: volume = length × width^2 × 0.5. Mice were euthanized on day 15 after seed implantation (Fig. 7A). Tumor specimens were weighted and then frozen or fixed in 4 % paraformaldehyde for histology assays.

Animal experiments were conducted in compliance with animal protocols approved by the Laboratory Animal Research Center of Soochow University. Animal testing and research conformed to all relevant ethical regulations. This research project was approved by the Ethics Committee of First People's Hospital of Changzhou (the Third Affiliated Hospital of Soochow University).

Tissue staining and analysis

Paraffin-embedded samples were cut into 4-μm sections and then used for hematoxylin and eosin (H&E) staining, immunohistochemistry staining, and TUNEL assay. H&E and immunohistochemistry staining were performed according to the routine techniques. TUNEL assay was performed using an *in situ* cell death detection kit (#11,684,817,910, Roche Diagnostics GmbH, Mannheim, Germany) and according to the manufacturer's protocol. The percentage of positive cells and relative integrated optical density (IOD) were calculated using Image-Pro Plus v 6.0 software (Media Cybernetics, Bethesda, MD, USA).

Frozen tumor sections were used for immunofluorescence detection of ROS. Frozen sections (10 μm) were incubated with 10 μM DCFH-DA in RPMI 1640 medium for 30 min at 37 °C, washed with RPMI 1640 medium, and then stained with DAPI. Relative fluorescence intensity was analyzed by ImageJ software.

Statistical analysis

Statistical analyses were performed only when ≥3 independent samples were acquired. All data presented in the figures were expressed as the mean ± standard deviation. Student's *t*-test or Wilcoxon rank sum test was applied when comparing the two groups. One-way ANOVA followed by Tukey's post-hoc test was applied when comparing multiple independent groups. When comparing the changes in tumor volume among multiple groups, repeated measures ANOVA was applied. A P value of <0.05 was considered to indicate a statistically significant difference. All analyses were performed using the SPSS 23.0 (IBM,

Armonk, NY, USA).

Results

CFZ sensitizes ESCC cells to ^{125}I seed radiation

We first evaluated the cytotoxicity of CFZ in Kyse-150 and EC-109 cells. As shown in Fig. 1B and Fig.S1, CFZ at low concentrations did not significantly affect cell viability within 24 h. The estimated IC_{10} values of CFZ at 24 h on Kyse-150 and EC-109 cells were 32.23 nM and 15.29 nM, respectively. According to the above results and previously published method [18], the CFZ-sensitizing concentration was determined to be 20 nM at 24 h. The anti-proliferative effect was evaluated using the EdU assay. CFZ alone barely affected cell proliferation in nonirradiated cells, but promoted ^{125}I seed radiation-induced inhibition of cell proliferation (Fig. 1C).

To further evaluate the radiosensitizing effect of CFZ, colony formation assay was performed. Considering prolonged drug treatment was highly toxic to cells (Fig. 1B), a lower concentration of CFZ (5 nM) was used. The sensitizer enhancement ratios for Kyse-150 and EC-109 cells were 1.804 and 1.787, indicating a significant radiosensitizing effect of CFZ (Fig. 1D). Radiobiological parameters of ESCC cells are shown in Table 1.

CFZ promotes ^{125}I seed radiation-induced apoptosis via the p53-independent pathway

Ionizing radiation (IR)-induced ROS overproduction and DNA damage are the core mechanisms by which IR inhibits and kills tumor cells [19]. Thus, we first investigated the synergistic effects of ^{125}I seed radiation and CFZ on ROS production and DNA damage in Kyse-150 and EC-109 cells. DCFH-DA probe was used to detect the changes in total intracellular ROS. The results revealed that ^{125}I seed radiation induced ROS production, and the combined treatment further elevated ROS levels (Fig. 2A). DNA damage was assessed by measuring the protein levels of phosphorylated H2AX. The results demonstrated that CFZ significantly aggravated ^{125}I seed radiation-induced DNA damage (Fig. 2C). Moreover, KEGG analysis of mRNA sequencing showed that combined treatment downregulated pathways associated with DNA repair, including DNA replication, base excision repair, nucleotide excision repair, mismatch repair, and homologous recombination (Table. S6).

Apoptosis is the primary cell death modality following DNA strand breaks [19]. Annexin V-FITC/PI assay showed that 20 nM CFZ did not promote apoptosis but significantly augmented the pro-apoptotic effect of ^{125}I seed radiation in both cell lines (^{125}I + CFZ *vs.* ^{125}I: 28.6 ± 1.3 % *vs.* 13.3 ± 0.4 % in Kyse-150 cells, 42.3 ± 1.2 % *vs.* 21.8 ± 1.2 % in EC-109 cells; Fig. 2B). Next, we investigated the apoptotic pathways by Western blot analysis (Fig. 2D and Fig. S2). The results showed that ^{125}I seed radiation increased protein expression of cleaved caspase-9, cleaved caspase-8, cleaved caspase-3, and cleaved PARP, indicating both death receptor-mediated and mitochondria-mediated apoptosis pathways were activated. The combined treatment further elevated protein levels of cleaved caspase-9, cleaved caspase-3, and cleaved PARP, but had little influence on cleaved caspase-8. These data indicate that CFZ augmented ^{125}I seed radiation-induced apoptosis via the mitochondrial pathway, but not via the death receptor pathway.

We also assessed the p53 pathway, which plays a key role in the activation of the mitochondrial apoptotic pathway following DNA damage. Baseline levels of p53 protein were significantly higher in Kyse-150 cells than in EC-109 cells (Fig 2E and Fig. S2). ^{125}I seed radiation activated the p53 pathway in both cell lines, however, CFZ inhibited radiation-activated p53 pathway by downregulating protein levels of p53 and phosphorylated p53 (Fig 2F and Fig. S2). Taken together, CFZ promotes ^{125}I seed radiation-induced mitochondrial apoptosis via the p53-independent pathway.

Table 1
Radiobiological parameters of esophageal squamous cell carcinoma cells.

	D_0 (Gy)	D_q (Gy)	N	SF_6	SER
Kyse-150					
^{125}I	2.012	1.406	2.011	0.099	
^{125}I+CFZ	1.115	1.420	3.573	0.016	1.804
EC-109					
^{125}I	2.007	2.510	3.492	0.165	
^{125}I+CFZ	1.123	2.044	6.174	0.029	1.787

The values of D_0, D_q, N, and SER were determined using the multi-target single-hit model. D_0, mean inactivation dose; D_q, quasi-threshold dose; N, extrapolation number; SF_6, survival fraction at 6 Gy; SER, sensitizer enhancement ratio. SER = $D_0(^{125}I)/D_0(^{125}I+CFZ)$.

CFZ promotes ^{125}I seed radiation-induced ERS and paraptosis

Previous studies found that paraptosis is an important mechanism of cell death induced by ^{125}I seed radiation [11,20]. Thus, we investigated the pro-paraptotic effect of ^{125}I seed radiation and CFZ on ESCC cells. We first assessed paraptosis by cell morphology, since paraptosis is characterized by cytoplasmic vacuolation. As shown in Fig. 3A, 20 nM CFZ had little influence on the cellular morphology but slightly increased the number of vacuolated cells. In a portion of Kyse-150 and EC-109 cells, ^{125}I seed radiation resulted in increased cell size and extensive cytoplasmic vacuolation surrounding the cell nucleus. Compared with ^{125}I seed radiation, the combined treatment led to more extensive and intense cytoplasmic vacuolation, leading to a higher proportion of vacuolated cells. Moreover, combined treatment-induced cytoplasmic vacuolization was attenuated by the paraptosis inhibitor CHX (10 μM).

To further confirm the pro-paraptotic effects of CFZ to ^{125}I seed radiation, we investigated intracellular Ca^{2+} homeostasis and ERS, which have been demonstrated to critically contribute to paraptosis [10,21]. The results revealed that ^{125}I seed radiation increased cytosolic Ca^{2+} levels, and co-treatment with CFZ further increased cytosolic and mitochondrial Ca^{2+} levels in both cell lines (Fig. 3B and 3C). CFZ barely affected the accumulation of ubiquitin-tagged proteins, but combined treatment significantly increased protein ubiquitination. Moreover, CFZ aggravated ^{125}I seed radiation-induced ERS (upregulation of Bip), and the combined treatment notably activated three canonical pathways of the UPR (upregulation of p-eIF2α, IRE1α, ATF6, and CHOP) in both cell lines (Fig. 3D and Fig. S3). However, the combined treatment did not reduce protein levels of Alix (Fig. 3E and Fig. S3), which has been reported to inhibit the onset of paraptosis. These results collectively indicated that CFZ promotes ^{125}I seed radiation-induced ERS and paraptosis.

Combined treatment of ^{125}I seed radiation and CFZ induces CHOP-mediated apoptosis

As CHOP has been reported to contribute to ^{125}I seed radiation-induced apoptosis in hepatocellular carcinoma cells, its role in the combined treatment-induced cell death was further investigated in Kyse-150 cells. First, we focused on the role of CHOP in apoptotic pathways (Fig. 4C and Fig. S4). siRNA was used to silence the *CHOP* gene, and CHOP protein expression induced by the combined treatment was significantly reduced. In cells receiving combined treatment, *CHOP* silencing downregulated the mitochondrial pathway (downregulation of cleaved caspase-9), upregulated the death receptor pathway (upregulation of cleaved caspase-8), and ultimately inhibited the execution of apoptosis (downregulation of cleaved caspase-3 and cleaved PARP). Next, we focused on changes in cell morphology (Fig. 4A and 4B). In cells treated with ^{125}I seed radiation or ^{125}I seed radiation + CFZ, *CHOP* silencing aggravated cytoplasmic vacuolation and slightly increased the proportion of vacuolated cells. Changes in cell morphology suggested an

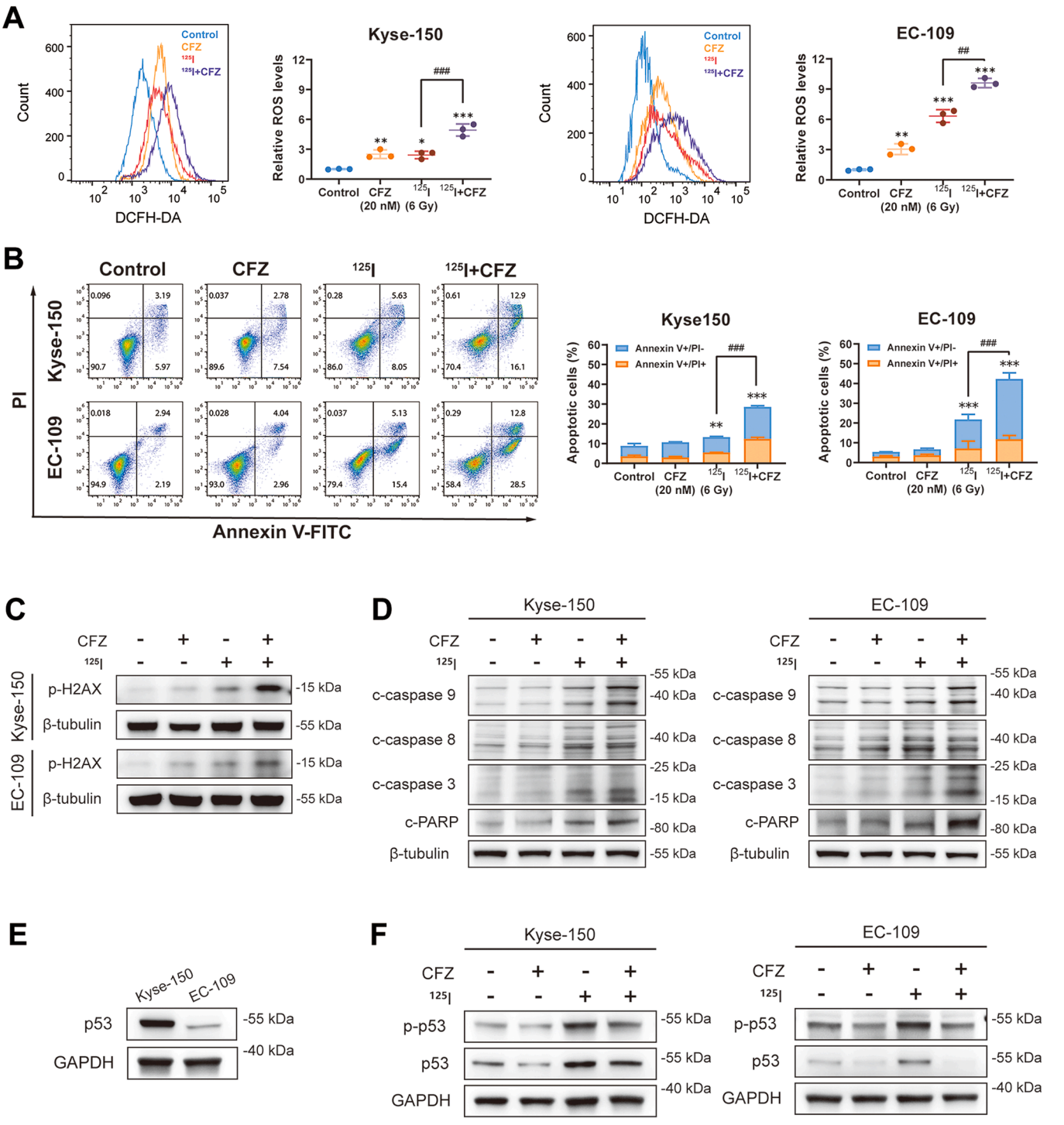

Fig. 2. CFZ enhances the pro-apoptotic effect of ^{125}I seed radiation in ESCC cells. Cells were treated with ^{125}I seed radiation (6 Gy) and CFZ (20 nM, 24 h) alone or in combination. (A) Combined treatment of ^{125}I seed radiation and CFZ induced ROS production in Kyse-150 and EC-109 cells. After the treatment, cells were stained with DCFH-DA and quantitatively analyzed by mean fluorescence intensity using flow cytometry. (B) Combined treatment of ^{125}I seed radiation and CFZ increased apoptotic cell number in Kyse-150 and EC-109 cells. After the treatment, apoptotic cells were detected by Annexin V-FITC/PI assay and quantitatively analyzed using flow cytometry. (C and D) CFZ promoted ^{125}I seed radiation-induced DNA damage and apoptotic pathway activation in Kyse-150 and EC-109 cells. After the treatment, protein levels of p-H2AX, cleaved caspase-9, cleaved caspase-8, cleaved caspase-3, cleaved-PARP, and β-tubulin (control for loading) were analyzed by Western blot. (E) Protein levels of p53 in untreated Kyse-150 and EC-109 cells were analyzed by Western blot. (F) Co-treatment with CFZ inhibited ^{125}I seed radiation-induced activation of the p53 pathway in Kyse-150 and EC-109 cells. After the treatment, protein levels of p-p53, p53, and GAPDH (control for loading) were analyzed by Western blot. $N = 3$, $^{*}P < 0.05$, $^{**}P < 0.01$, and $^{***}P < 0.001$ compared to control group. $^{\#\#}P < 0.01$ and $^{\#\#\#}P < 0.001$ compared between indicated groups.

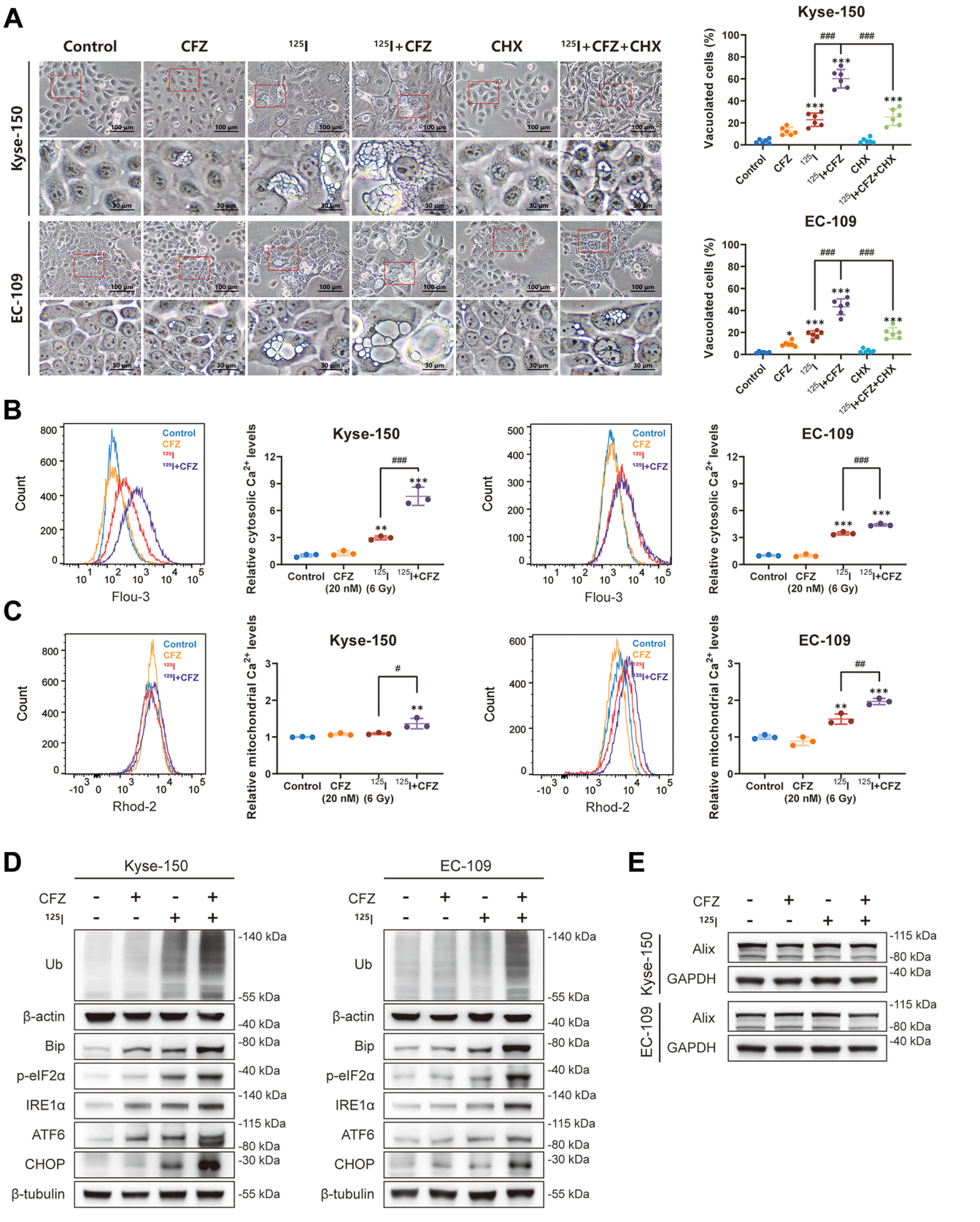

(caption on next page)

Fig. 3. CFZ enhances the pro-paraptotic effect of ^{125}I seed radiation in ESCC cells. (A) CFZ aggravated ^{125}I seed radiation-induced cytoplasmic vacuolation in Kyse-150 and EC-109 cells. Cells were treated with CFZ (20 nM, 24 h), ^{125}I seed radiation (6 Gy), and CHX (10 μM, 24 h) alone or in combination. Cell morphological changes were observed under light microscopy, and the percentage of vacuolated cells was measured. Scale bar (upper) = 100 μm, Scale bar (lower) = 30 μm. $N = 6$. (B and C) Combined treatment of ^{125}I seed radiation and CFZ increased cytosolic and mitochondrial Ca^{2+} levels in Kyse-150 and EC-109 cells. Cells were treated with ^{125}I seed radiation (6 Gy) and CFZ (20 nM, 24 h) alone or in combination, then stained with Fluo-3 AM or Rhod-2 AM and quantitatively analyzed by mean fluorescence intensity using flow cytometry. (D) CFZ aggravated ^{125}I seed radiation-induced ubiquitination, ER stress, and UPR in Kyse-150 and EC-109 cells. Cells were treated with ^{125}I seed radiation (6 Gy) and CFZ (20 nM, 24 h) alone or in combination. Protein levels of Ub, β-actin (control for loading), Bip, p-eIf2α, IRE1α, ATF6, CHOP, and β-tubulin (control for loading) were analyzed by Western blot. (E) Combined treatment of ^{125}I seed radiation and CFZ did not influence the protein expression of Alix as analyzed by Western blot. $N = 3$, $^{*}P < 0.05$, $^{**}P < 0.01$, and $^{***}P < 0.001$ compared to control group. $^{\#}P < 0.05$, $^{\#\#}P < 0.01$, and $^{\#\#\#}P < 0.001$ compared between indicated groups.

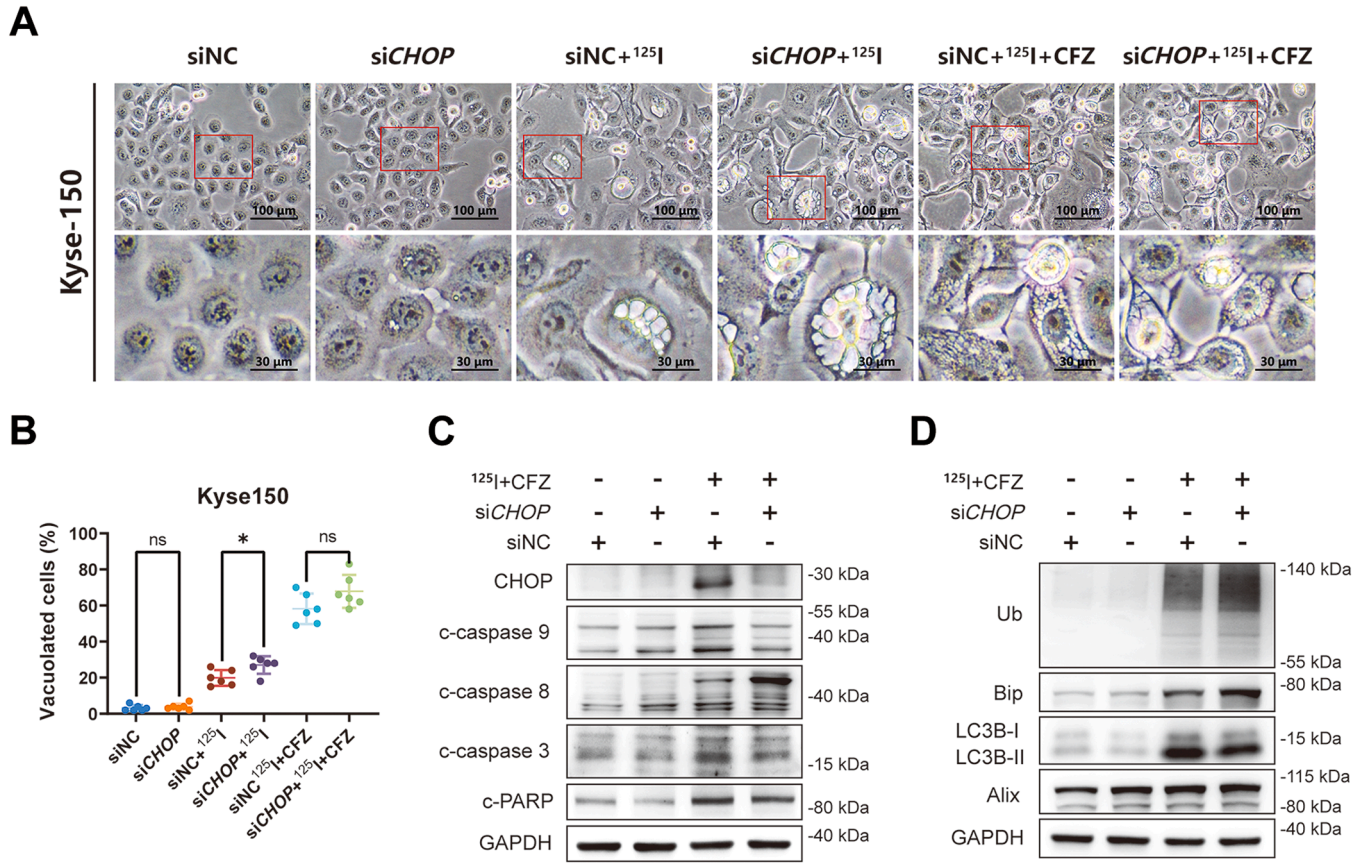

Fig. 4. Combined treatment of ^{125}I seed radiation and CFZ induces CHOP-mediated apoptosis in Kyse-150 cells. (A and B) Knockdown of *CHOP* aggravated ^{125}I seed radiation-induced cytoplasmic vacuolation. Cells were transfected with *CHOP*-specific siRNA or non-specific control, and then treated with ^{125}I seed radiation (6 Gy) or ^{125}I seed radiation (6 Gy) + CFZ (20 nM, 24 h). Cell morphological changes were observed under light microscopy, and the percentage of vacuolated cells was measured. Scale bar (upper) = 100 μm, Scale bar (lower) = 30 μm. $N = 6$, $^{*}P < 0.05$ compared between indicated groups. ns, not significant. (C and D) Knockdown of *CHOP* alleviated combined treatment-induced apoptosis, but aggravated ERS. Cells were transfected with *CHOP*-specific siRNA or non-specific control, and then treated with ^{125}I seed radiation (6 Gy) + CFZ (20 nM, 24 h). Protein levels of CHOP, cleaved caspase-9, cleaved caspase-8, cleaved caspase-3, cleaved-PARP, Ub, Bip, LC3B, Alix, and GAPDH (control for loading) were analyzed by Western blot. $N = 4$.

increase in ERS, which was further verified by Western blot analysis (Fig. 4D and Fig. S4). In cells receiving combined treatment, *CHOP* silencing significantly increased protein levels of ubiquitin and Bip, indicating that CHOP was beneficial to alleviating ERS. Since CHOP is involved in the formation of autophagosomes, we evaluated autophagy by LC3B-II, a marker for the formation of autophagosomes. The result showed that *CHOP* silencing reduced LC3B-II expression. Besides, protein levels of Alix were also evaluated, but no significant changes were observed. These findings indicated that combined treatment of ^{125}I seed radiation and CFZ induces CHOP-mediated apoptosis in Kyse-150 cells, and CHOP is critical for alleviating ERS.

Analysis results of DEGs

To verify and gain some insights into the molecular mechanisms by which the combination therapy inhibited cell proliferation and promoted cell death, we conducted mRNA sequencing analysis on Kyse-150 cells treated with or without combined treatment. A total of 2957 DEGs were identified, including 1512 upregulated DEGs and 1445 downregulated DEGs (Fig. S5A). GO functional analysis and KEGG pathway analysis were performed based on these DEGs. GO analysis showed that response to unfolded protein was the most significantly upregulated biological process, and misfolded protein binding and unfolded protein binding were the most significantly upregulated molecular functions (Fig. 5A and Table S1–3). KEGG analysis showed that ferroptosis, mitophagy, NF-kappa B signaling pathway, TNF signaling pathway, MAPK signaling pathway, and protein processing in endoplasmic reticulum were significantly upregulated in treated cells, while p53 pathway, cell cycle, DNA replication, and base excision repair were significantly downregulated (Fig. 5B and Table S4–6).

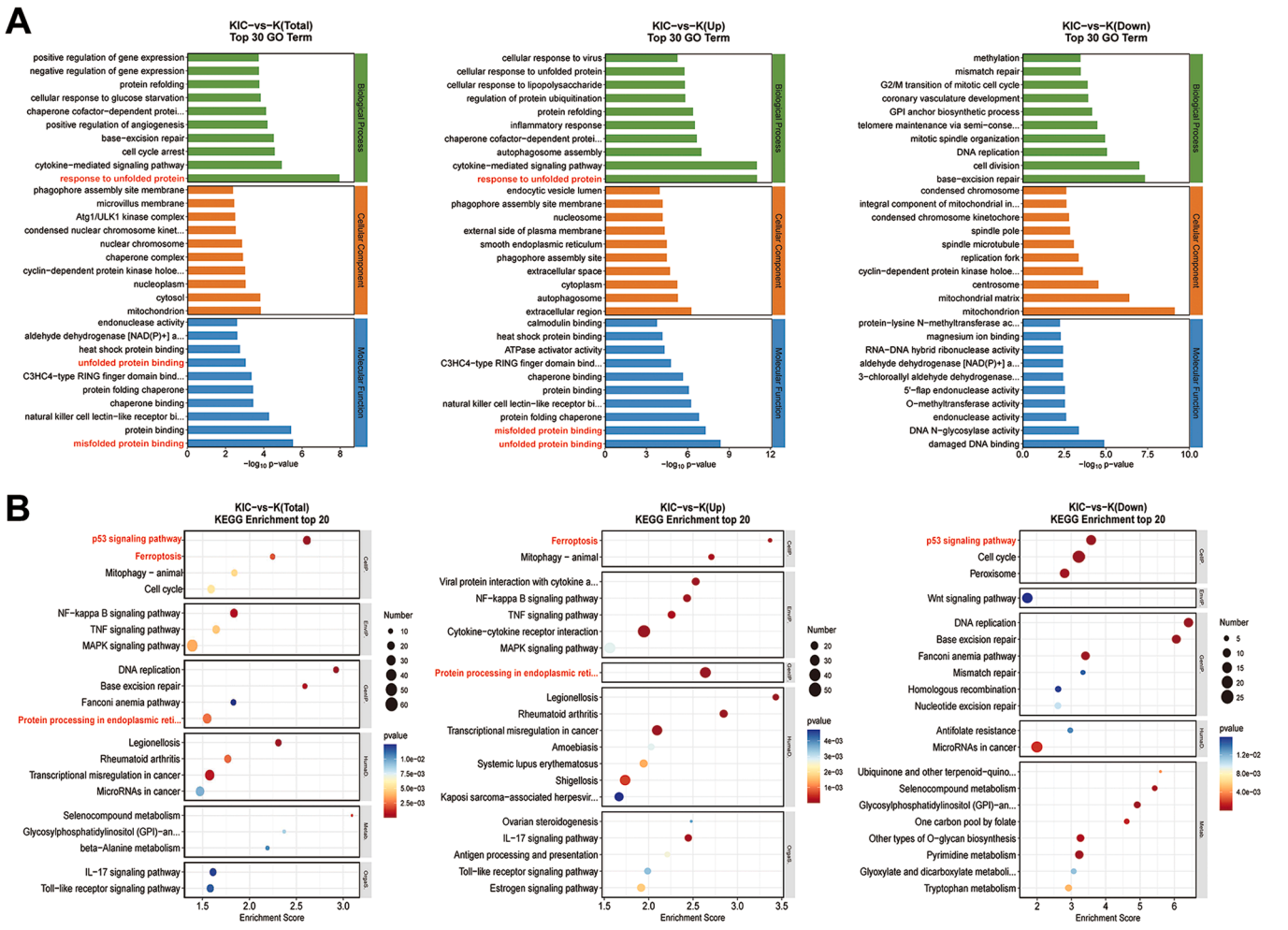

Fig. 5. Results of transcriptome analysis of Kyse-150 cells treated with combined treatment compared to untreated cells. (A) Top 30 total, upregulated and downregulated terms based on GO functional enrichment analysis of DEGs. (B) Top 20 total, upregulated and downregulated pathways based on KEGG pathway enrichment analysis of DEGs. Terms and pathways relevant to this study are marked in red.

Combined treatment of ^{125}I seed radiation and CFZ induces ferroptosis in ESCC cells

As KEGG analysis indicated that ferroptosis pathway was the most significantly upregulated cellular process (Fig. 5B and Table S5), we further investigated ferroptosis and its molecular mechanisms in both cell lines. Ferroptosis is an iron-dependent form of cell death, therefore treatment-induced changes of intracellular Fe^{2+} were first detected. As shown in Fig. 6A, combined treatment significantly promoted the accumulation of intracellular Fe^{2+}, which was reversed partially by the iron chelator, DFO (20 μM). Lipid peroxidation is a key event of ferroptosis. Next, we assessed cellular lipid peroxide (Fig. 6B). ^{125}I seed radiation significantly promoted lipid peroxide production and CFZ further elevated lipid peroxide levels. Fer-1 (10 μM), as a lipid peroxide scavenger, slightly alleviated combined treatment-induced lipid peroxide accumulation. Moreover, both DFO (20 μM) and Fer-1 (10 μM) partially reduced combined treatment-induced cell death (Fig. 6C). These findings indicated that combined treatment of ^{125}I seed radiation and CFZ induces ferroptosis in ESCC cells.

The expression of ferroptosis-related genes obtained by mRNA sequencing was analyzed to investigate the underlying mechanism of combined treatment-induced ferroptosis. As shown in the heat map (Fig. 6D and Table S7) and KEGG network path diagram (Fig. S5B), combined treatment affected the antioxidant defense system, iron metabolism, mitochondrial metabolism, and promoted the synthesis of polyunsaturated fatty acid-containing phospholipid (PUFA-PL). Three sources of intracellular Fe^{2+} were significantly increased, including ferritin degradation via autophagy (upregulation of *FTH1, MAP1LC3B, NCOA4*), upregulation of metal transporter (upregulation of *SLC39A14*), and heme degradation through catalysis by HO-1 (upregulation of *HMOX1*). System Xc^--GPX4 axis is the primary defensive weapon of the lipid antioxidant system [22], and its dysfunction was found at the transcriptional level, manifested by the upregulation of *SLC7A11* and the downregulation of *GPX4*. Next, proteins related to iron metabolism and system Xc^--GPX4 were verified (Fig. 6E and Fig. S6). ^{125}I seed radiation only slightly promoted the expression of LC3B-II, SLC39A14, and HO-1, while co-treatment with CFZ significantly elevated levels of these proteins. Both ^{125}I seed radiation and combined treatment promoted SLC7A11 expression. In EC-109 cells, SLC7A11 expression was higher in the combined treatment group than in the ^{125}I seed radiation group. However, no significant difference was found in Kyse-150 cells. ^{125}I seed radiation significantly promoted GPX4 expression, which was attenuated markedly by co-treating with CFZ in both cell lines. These results collectively indicated that combined treatment of ^{125}I seed radiation and CFZ induces ferroptosis by promoting the accumulation of intracellular $Fe^{2+}$and downregulating GPX4 expression.

CFZ enhances the anticancer effect of ^{125}I seed radiation in vivo

To evaluate the therapeutic effect of the combination therapy, the Kyse-150 cell xenograft mouse model was used (Fig. 7A). Both ^{125}I seed radiation and combined treatment led to significantly smaller tumor

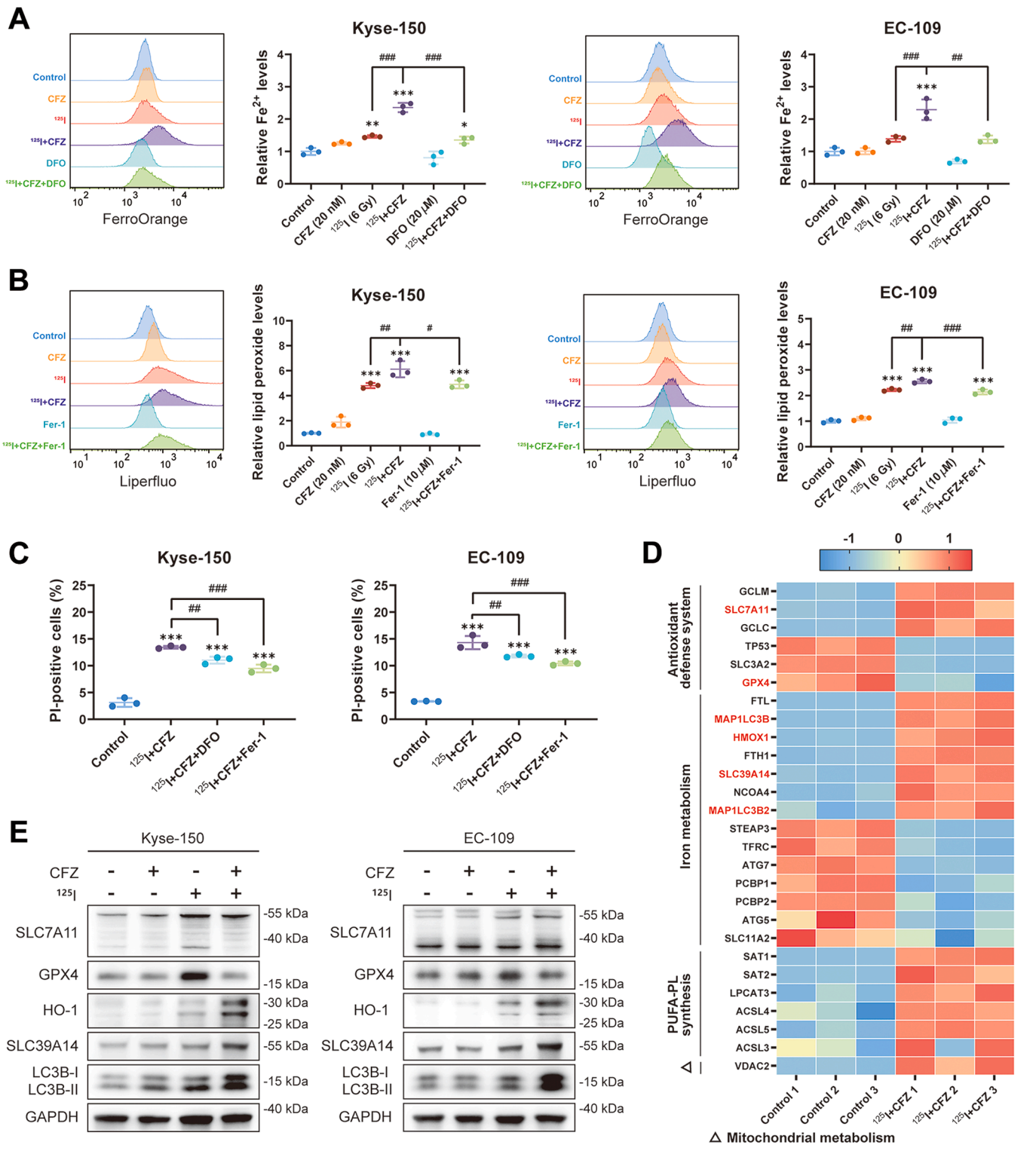

Fig. 6. Combined treatment of ^{125}I seed radiation and CFZ induces ferroptosis in ESCC cells. (A) Combined treatment induced intracellular Fe^{2+} overload in Kyse-150 and EC-109 cells. Cells were treated with CFZ (20 nM, 24 h), ^{125}I seed radiation (6 Gy), and DFO (20 μM, 24 h) alone or in combination. Then, cells were stained with the FerroOrange probe and quantitatively analyzed by mean fluorescence intensity using flow cytometry. (B) Combined treatment promoted lipid peroxidation in Kyse-150 and EC-109 cells. Cells were treated with CFZ (20 nM, 24 h), ^{125}I seed radiation (6 Gy), and Fer-1 (10 μM, 24 h) alone or in combination. Then, cells were stained with the Liperfluo probe and quantitatively analyzed by mean fluorescence intensity using flow cytometry. (C) Ferroptosis inhibitors alleviated combined treatment-induced cell death in Kyse-150 and EC-109 cells. Cells were treated with ^{125}I seed radiation (6 Gy) + CFZ (20 nM, 24 h) alone or in combination with DFO (20 μM, 24 h) or Fer-1 (10 μM, 24 h), and then stained with PI and quantitatively analyzed using flow cytometry. (D) Heatmap of mRNA sequencing data of the key genes involved in ferroptosis pathways. (E) Proteins related to system Xc^--GPX4 and iron metabolism were verified in Kyse-150 and EC-109 cells. Cells were treated with ^{125}I seed radiation (6 Gy) and CFZ (20 nM, 24 h) alone or in combination. Protein levels of SLC7A11, GPX4, HO-1, SLC39A14, LC3B, and GAPDH (control for loading) were analyzed by Western blot. $N = 3$, $^{*}P < 0.05$, $^{**}P < 0.01$, and $^{***}P < 0.001$ compared to control group. $^{\#}P < 0.05$, $^{\#\#}P < 0.01$, and $^{\#\#\#}P < 0.001$ compared between indicated groups.

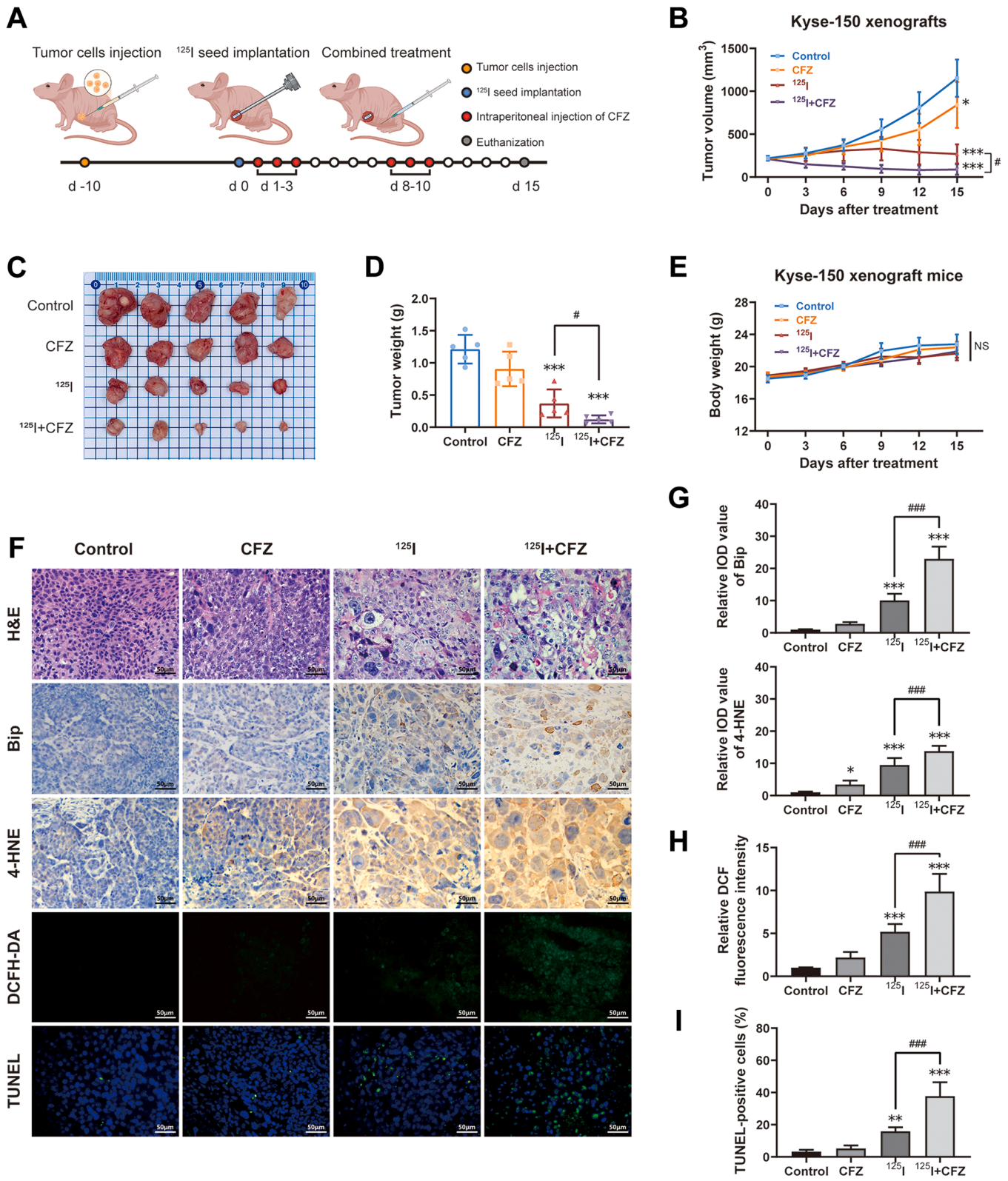

Fig. 7. CFZ enhances the anticancer effect of ^{125}I seed radiation *in vivo*. Nude mice bearing Kyse-150 tumor xenografts ($N = 5$) underwent ^{125}I seed implantation and then were injected intraperitoneally daily with vehicle solution or CFZ (0.425 mg/kg) for 3 consecutive days followed by a 4-day rest period. Mice were sacrificed on day 15, and their tumors were harvested and weighed. (A) Schematic diagram of animal experiments. (B) Changes in tumor volume after seed ^{125}I seed implantation. (C) Photograph and (D) tumor weights of harvested tumors. (E) Changes in body weight of nude mice after seed ^{125}I seed implantation. (F) H&E staining, immunohistochemical staining, immunofluorescence staining, and TUNEL assay of harvested tumor specimens. Scale bar = 50 μm. (G) Immunohistochemical staining of Bip and 4-HNE was analyzed in relative integrated optical density (IOD) value. (H) Immunofluorescence staining of ROS was analyzed in relative DCF fluorescence intensity. (I) TUNEL assay was analyzed in the percentage of positive cells. $^{*}P < 0.05$, $^{**}P < 0.01$, and $^{***}P < 0.001$ compared to control group. $^{\#}P < 0.05$ and $^{\#\#\#}P < 0.001$ compared between indicated groups. ns, not significant.

volumes (Fig. 7B and 7C) and lower tumor weights (Fig. 7D). Compared with the ^{125}I seed radiation alone, the combined treatment showed better effect on the reduction of tumor volumes and tumor weights. No drugs or radiation caused obvious toxicity as assessed by the body weight of the treated mice (Fig. 7E). H&E staining showed that cell density was lower in the irradiated tumor samples (the ^{125}I and combined treatment group) than in nonirradiated tumor samples (the control and CFZ group). Moreover, more vacuolated-like cells were observed in the irradiated tumor samples, especially in the combined treatment group (Fig. 7F). Tissue ERS and lipid peroxidation were measured by immunohistochemistry staining of Bip and 4-HNE, and increased tissue ERS and lipid peroxidation were observed in irradiated tumor samples (Fig. 7F and 7G). Tissue ROS production was measured by DCFH-DA staining, which showed increased ROS levels in irradiated tumor samples (Fig. 7F and 7H). Notably, compared with ^{125}I seed radiation monotherapy, co-treatment with CFZ generated more tissue ROS, lipid peroxides, and ERS, and further promoted cell death (TUNEL assay, Fig. 7F and 7I). These results corroborate the *in vitro* data, demonstrating that CFZ promotes ^{125}I seed radiation-induced generation of ROS, lipid peroxides, and ERS, thereby enhancing the anticancer effect.

Discussion

Radiation therapy is one of the primary treatments for malignant tumors. Most types of radiation therapies such as external radiation therapy use the high-dose-rate (HDR) irradiation pattern. ^{125}I seed brachytherapy adopts the CLDR irradiation pattern, which emits X-rays and γ-rays with a half-life of 59.4 days. ^{125}I seed brachytherapy follows the inverse square law, making it deliver high radiation doses to the tumor, but relative sparing of surrounding normal tissues. ^{125}I seed brachytherapy is well-established for the treatment of prostate cancer [23]. In the past 20 years, ^{125}I seed brachytherapy has been applied to treat various malignant tumors [4]. Radioresistance, especially apoptosis resistance, of tumor cells is an important cause of the failure of radiation therapy. Although ^{125}I seed brachytherapy increases the local cumulative dose, it cannot overcome the radioresistance of tumor cells. To improve the efficacy of ^{125}I seed brachytherapy, it is necessary to study radiosensitizers and their mechanisms. Herein, we evaluated the sensitizing effect of proteasome inhibitor, CFZ, on ^{125}I seed radiation in ESCC cells. Our data showed that the combined treatment of ^{125}I seed radiation and CFZ can effectively inhibit tumor cell proliferation and induce multiple modalities of cell death.

Apoptosis is the main type of regulated cell death induced by ^{125}I seed radiation and the main target of sensitization therapy. Several drugs, including salinomycin [24], lobaplatin [12], and scutellarin [25], as well as oxygenation nanomaterials [26] have demonstrated good ability to promote ^{125}I seed radiation-induced apoptosis in preclinical studies. DNA damage, especially double-strand breaks, is the primary cause of IR-induced apoptosis. DNA can be damaged directly by IR or indirectly by IR-induced ROS. After DNA damage, ATM/ATR is activated and phosphorylates the transcription factor p53. The activated p53 triggers apoptosis through multiple pathways [27]. In addition to DNA damage, ^{125}I seed radiation can phosphorylate p53 via the p38 MAPK pathway [28]. In line with previous studies [24,28], we also found that ^{125}I seed radiation aggravated DNA damage and increased p53 expression and phosphorylation. Nevertheless, although CFZ promoted ^{125}I seed radiation-induced DNA damage and apoptosis, CFZ inhibited ^{125}I seed radiation-induced p53 expression and phosphorylation. These results indicated that CFZ promotes ^{125}I seed radiation-induced apoptosis independent of p53 activation, and combined treatment promoted apoptosis in other ways.

^{125}I seed radiation not only damages DNA but also interferes with the ER, causing ERS and UPR-mediated apoptosis. It has been well established that ROS-dependent damage is the main driver of IR-induced biological effects. Importantly, ROS is a critical cause of ERS, as it causes oxidative damage to proteins, leading to proteostasis imbalance [29,30]. In our previous study [11], ^{125}I seed radiation led to ER swelling and upregulation of the ERS marker in ESCC cells. Besides, reducing ROS attenuated ^{125}I seed radiation-induced ERS and apoptosis. Li, D. et al. [12] found that ^{125}I seed radiation promoted apoptosis by upregulating the PERK-eIF2α-ATF4-CHOP pathway in hepatocellular carcinoma cells. The ERS and UPR are important ways for ^{125}I seed radiation-induced apoptosis, but ERAD hinders the aggravation of ERS. In this study, we inhibited ERAD with the irreversible proteasome inhibitor, CFZ. Combined treatment of ^{125}I seed radiation and CFZ significantly aggravated ERS, upregulated three UPR pathways, increased CHOP expression, and promoted apoptosis via the mitochondrial pathway. *CHOP* silencing led to the downregulation of the mitochondrial apoptotic pathway in Kyse-150 cells, further confirming that CFZ promotes ^{125}I seed radiation-induced mitochondrial apoptosis via the UPR-CHOP pathway.

Paraptosis is another form of cell death associated with ERS and it has been found in ^{125}I seed-irradiated cells [20]. The characteristic of paraptosis is dilation of the ER and/or mitochondria, which causes extensive cytoplasmic vacuolation and ultimately leads to cell lysis [10]. Paraptosis appears to be a backup death pathway for cells with impaired apoptotic response [9,31]. Perturbations of Ca^{2+} homeostasis and cellular proteostasis have been proposed to induce stress in the ER and mitochondria, thereby contributing to paraptosis [21]. In Kyse-150 and EC-109 cells, ^{125}I seed radiation and co-treatment with CFZ led to the paraptosis-like cell morphology, and paraptosis was further confirmed by intracellular Ca^{2+} levels, protein ubiquitination, and ERS. Compared with ^{125}I seed radiation, the combined treatment led to higher levels of paraptosis. As a specific and convergent transcription factor for ERS, CHOP was reported to contribute to ER-derived vacuolation and subsequent paraptosis in colon cancer cells treated with loperamide and bortezomib (Bortezomib) [32]. Seo, MJ. et al. [18] found that ATF4, but not CHOP, played a critical role in the paraptosis in bortezomib (Bortezomib)-treated breast cancer cells. In this study, *CHOP* silencing aggravated ERS and cytoplasmic vacuolation but inhibited autophagy, suggesting that CHOP contributes to protecting ESCC cells from ERS and paraptosis. This phenomenon could be attributed to two reasons. Firstly, CHOP positively regulates autophagy, which functions as a noncanonical ERAD pathway [33]. *CHOP* silencing impaired autophagy, thereby aggravating ERS. Secondly, *CHOP* silencing inhibited ERS-mediated apoptosis, thereby resulting in the survival of cells with high ERS levels and increasing overall ERS levels. mRNA sequencing analysis was performed to reveal the underlying mechanisms comprehensively. In addition to reconfirmation that the combined treatment aggravated ERS, promoted UPR, and downregulated the p53 pathway, we unexpectedly found that combined treatment significantly upregulated the ferroptosis pathway. Ferroptosis is a form of regulated cell death driven by iron-dependent phospholipid peroxidation. Iron metabolism (increase in labile iron pool), synthesis and peroxidation of PUFA-PLs, and mitochondrial metabolism are three core mechanisms constituting the main prerequisites driving ferroptosis [34]. ROS peroxidizes PUFA-PLs to phospholipid hydroperoxide, which is considered to be the enforcer of ferroptosis [22]. KEGG analysis indicated that the combined treatment mainly affected iron metabolism and synthesis and peroxidation of PUFA-PLs. Scholars have recently conducted systematic studies on ferroptosis induced by HDR IR [35–37]. HDR IR, represented by X-ray radiation therapy, causes lipid peroxidation and ferroptosis by inducing ROS production and upregulating ACSL4 expression [35]. However, HDR IR also upregulates the System Xc^--GPX4 antioxidant axis, so HDR IR only induces low levels of ferroptosis [35,37]. Ferroptosis inducers targeting a single ferroptosis mechanism show good synergistic effects with HDR radiation therapy [38]. The degree and mechanism of ferroptosis induced by CLDR radiation are still blind spots of current research. This study provided a preliminary exploration of ferroptosis induced by ^{125}I seed CLDR radiation. ^{125}I seed radiation led to increases in intracellular Fe^{2+} levels and lipid peroxide, two critical mechanisms

of ferroptosis. Acting as a ferroptosis inducer, CFZ promoted ^{125}I seed radiation-induced intracellular Fe^{2+} overload and lipid peroxidation, and cell death triggered by the combined treatment was partially counteracted by ferroptosis inhibitors, Fer-1 and DFO. These results confirmed the ferroptosis induction effect of combination therapy.

The increase in the labile iron pool is regulated by multiple mechanisms, such as HO-1-mediated heme degradation, upregulation of metal transporters (for example, SLC39A14), and autophagy-mediated ferritin degradation [39]. ERS and UPR pathways are documented to be involved in regulating HO-1, SLC39A14, and autophagy. HO-1 is an ER-anchored enzyme that metabolizes heme into Fe^{2+}, and the HO-1 can be upregulated by the pathway mediated by ER transmembrane protein PERK [40]. Metal transporter SLC39A14 mediates the transport of Zn^{2+}, Fe^{2+}, and Mn^{2+} into cells. ERS causes an increase in *SLC39A14* gene expression via activation of the transcription factors ATF4 and ATF6α [41]. UPR regulates and interacts with autophagy through multiple pathways. The PERK-eIF2α-ATF4 pathway is essential for the transcription of autophagy genes, such as *SQSTM1, ATG5, ATG7*, and *ATG10* [8]. Our data indicated that the combined treatment upregulated the expression of HO-1 and SLC39A14 and promoted autophagy, which could be the main causes of the increase in the labile iron pool.

The system Xc^--GPX4 antioxidant axis is the most classical lipid antioxidant mechanism and the main target of current ferroptosis inducers [42]. Both ^{125}I seed radiation and the combined treatment increased the expression of SLC7A11, the transporter subunit in system Xc^-, but the difference between these two groups was not significant. Consistent with HDR IR, ^{125}I seed CLDR radiation significantly increased GPX4 expression. Interestingly, increased expression of GPX4 was downregulated markedly by the co-treatment with CFZ. mRNA sequencing analysis indicated that combined treatment downregulated *GPX4* at the transcriptional level. Transcription factors have been reported to regulate GPX4 expression including C/EBP, CREB, ELK1, IRF1, AP-1, Nrf2, NF-Y, Sp1, and TFAP2c [22,43–46]. Among these transcription factors, genes of AP-1, Sp1, and TFAP2c were differentially expressed and their changes were consistent with the regulation of GPX4 (Table S8). Based on this, AP-1, Sp1, and TFAP2c could participate in the downregulation of *GPX4*. On the other hand, whether CFZ is involved in the degradation or depletion of GPX4 protein requires further investigation. Collectively, this study conducted preliminary mechanism exploration on ferroptosis triggered by ^{125}I seed radiation and the combined treatment in ESCC cells. CFZ was shown to boost ^{125}I seed radiation-induced ferroptosis through multiple mechanisms. Comprehensive mechanics of ferroptosis induced by ^{125}I seed CLDR radiation in cancer cells and the sensitization effect of the ferroptosis inducer on ^{125}I seed brachytherapy warrants further investigation.

Tumor cells themselves have multiple mechanisms of resistance to apoptotic stimuli, leading to radioresistance and tumor progression. Therefore, inducing multiple modalities of cell death is a more effective therapeutic strategy in cancer cells that have proven resistant to conventional pro-apoptotic treatments [47]. This is the first study evaluating the sensitization strategy that induces multiple cell death modalities for ^{125}I seed brachytherapy. This study demonstrated that CFZ significantly promotes ^{125}I seed radiation-induced cell death of ESCC by promoting apoptosis, paraptosis, and ferroptosis. ERS and UPR pathways participate in the regulation of these cell death modalities and play a central role in apoptosis and paraptosis (Fig. 8). In animal research, the combination therapy also effectively inhibited tumor growth and aggravated ERS, lipid peroxidation, and death of tumor cells. These results indicated that CFZ appears to be a promising approach to overcome radioresistance to ^{125}I seed brachytherapy. The sensitization strategy targeting ERS is expected to improve the efficacy of ^{125}I brachytherapy for esophageal cancer.

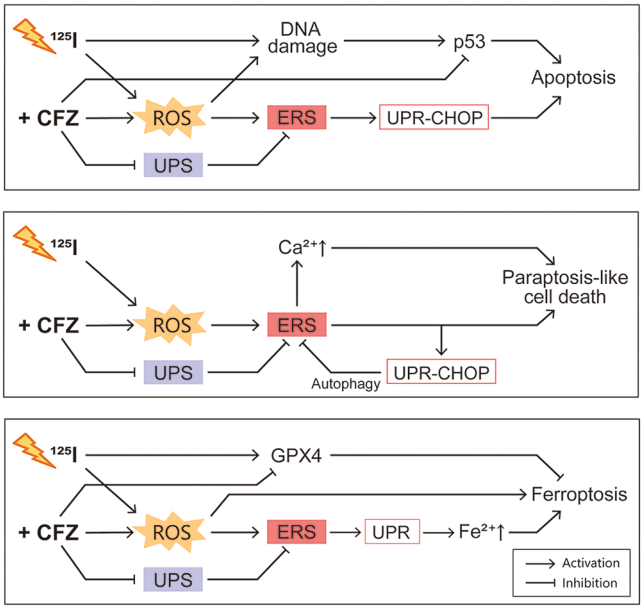

Fig. 8. Schematic illustration of the underlying mechanisms for the synergistic effect of ^{125}I seed radiation and CFZ in inducing apoptosis, paraptosis, and ferroptosis.

Funding

This study was funded by the Natural Science Foundation of Jiangsu Province (BK20210085), the Innovative and Entrepreneurial Talent Program of Jiangsu Province (No.202131592), and the Innovative Talent Introduction and Training Program of Changzhou (CQ20210110).

Ethics approval and consent to participate

All experiments involving mice were performed in compliance with animal protocols approved by the Laboratory Animal Research Center of Soochow University (Suzhou, China), and were approved by the Ethics Committee of First People's Hospital of Changzhou (No. 2022,017).

Consent for publication

All authors approved the final manuscript and the submission to this journal.

Data availability

The RNA-Seq dataset analyzed during the current study is available in the Sequence Read Archive (SRA) database (https://www.ncbi.nlm.nih.gov/sra/) with BioProject number PRJNA1111689. Other data in the current study are available from the corresponding author on reasonable request.

CRediT authorship contribution statement

Chao Wang: Methodology, Investigation, Writing – original draft, Methodology, Funding acquisition, Formal analysis. **Yin-Lin Zha:** Writing – original draft, Methodology, Investigation, Formal analysis. **Hao Wang:** Methodology, Investigation. **Bai Sun:** Methodology, Investigation. **Wei-Guang Qiang:** Methodology, Investigation. **Ye Yuan:** Visualization, Formal analysis, Data curation. **Hong-Bing Shi:** Writing – review & editing, Validation, Conceptualization. **Wen-Wei Hu:** Writing – review & editing, Supervision, Resources, Conceptualization.

Declaration of competing interest

The authors declare that they have no known competing financial interests or personal relationships that could have appeared to influence the work reported in this paper.

Acknowledgements

We thank OE Biotech, Inc., (Shanghai, China) for assisting in sequencing and bioinformatics analysis.

Supplementary materials

Supplementary material associated with this article can be found, in the online version, at doi:10.1016/j.tranon.2025.102393.

References

[1] H. Sung, J. Ferlay, R.L. Siegel, M. Laversanne, I. Soerjomataram, A. Jemal, F. Bray, Global Cancer statistics 2020: GLOBOCAN estimates of incidence and mortality worldwide for 36 cancers in 185 countries, *CA* Cancer J. Clin 71 (3) (2021) 209–249, https://doi.org/10.3322/caac.21660.

[2] E.C. Smyth, J. Lagergren, R.C. Fitzgerald, F. Lordick, M.A. Shah, P. Lagergren, D. Cunningham, Oesophageal cancer, Nat. Rev. Dis. Primers 3 (2017) 17048, https://doi.org/10.1038/nrdp.2017.48.

[3] J.E. Rogers, M. Sewastjanow-Silva, R.E. Waters, J.A. Ajani, Esophageal cancer: emerging therapeutics, Expert Opin. Ther. Targets 26 (2) (2022) 107–117, https://doi.org/10.1080/14728222.2022.2036718.

[4] S. Wei, C. Li, M. Li, Y. Xiong, Y. Jiang, H. Sun, B. Qiu, C.J. Lin, J. Wang, Radioactive Iodine-125 in tumor therapy: advances and future directions, Front. Oncol. 11 (2021) 717180, https://doi.org/10.3389/fonc.2021.717180.

[5] L. Wu, X. Zhao, S. Tian, K. Zhang, C. He, Y. Feng, J. Zhou, W. Guo, Z. Ji, X. He, et al., Efficacy and toxicity of Iodine-125 seed implantation for lymph node recurrence secondary to esophageal cancer after radiotherapy: a multicenter retrospective study, Radiat. Oncol. 18 (1) (2023) 18, https://doi.org/10.1186/s13014-022-02196-y.

[6] R. Dong, J. Lu, C.H. Zeng, H. Li, J.H. Guo, Safety and efficacy of computed tomography-guided iodine-125 brachytherapy as a salvage treatment for locoregional lymph node recurrence of esophageal cancer, J. Vasc. Interv. Radiol. 33 (11) (2022) 1399–1407, https://doi.org/10.1016/j.jvir.2022.07.017.

[7] J.H. Guo, G.J. Teng, G.Y. Zhu, S.C. He, W. Fang, G. Deng, G.Z. Li, Self-expandable esophageal stent loaded with 125I seeds: initial experience in patients with advanced esophageal cancer, Radiology. 247 (2) (2008) 574–581, https://doi.org/10.1148/radiol.2472070999.

[8] X. Chen, C. Shi, M. He, S. Xiong, X. Xia, Endoplasmic reticulum stress: molecular mechanism and therapeutic targets, Signal. Transduct Target. Ther. 8 (1) (2023) 352, https://doi.org/10.1038/s41392-023-01570-w.

[9] D. Kessel, J.J. Reiners, Photodynamic therapy: autophagy and mitophagy, apoptosis and paraptosis, Autophagy. 16 (11) (2020) 2098–2101, https://doi.org/10.1080/15548627.2020.1783823.

[10] C.C. Xu, Y.F. Lin, M.Y. Huang, X.L. Zhang, P. Wang, M.Q. Huang, J.J. Lu, Paraptosis: a non-classical paradigm of cell death for cancer therapy, Acta. Pharmacol. Sin. 45 (2) (2024) 223–237, https://doi.org/10.1038/s41401-023-01159-7.

[11] C. Wang, T.K. Li, C.H. Zeng, R. Fan, Y. Wang, G.Y. Zhu, J.H. Guo, Iodine-125 seed radiation induces ROS-mediated apoptosis, autophagy and paraptosis in human esophageal squamous cell carcinoma cells, Oncol. Rep. 43 (6) (2020) 2028–2044, https://doi.org/10.3892/or.2020.7576.

[12] D. Li, W.J. Wang, Y.Z. Wang, Y.B. Wang, Y.L. Li, Lobaplatin promotes (125)I-induced apoptosis and inhibition of proliferation in hepatocellular carcinoma by upregulating PERK-eIF2alpha-ATF4-CHOP pathway, Cell Death. Dis. 10 (10) (2019) 744, https://doi.org/10.1038/s41419-019-1918-1.

[13] X. Cao, Z. Yan, Z. Chen, Y. Ge, X. Hu, F. Peng, W. Huang, P. Zhang, R. Sun, J. Chen, et al., The emerging role of deubiquitinases in radiosensitivity, Int. J. Radiat. Oncol. Biol. Phys. 118 (5) (2024) 1347–1370, https://doi.org/10.1016/j.ijrobp.2023.12.003.

[14] E. Frisira, F. Rashid, S.N. Varma, S. Badodi, V.A. Benjamin-Ombo, D. Michod, M. V. Niklison-Chirou, NPI-0052 and gamma-radiation induce a synergistic apoptotic effect in medulloblastoma, Cell Death. Dis. 10 (11) (2019) 785, https://doi.org/10.1038/s41419-019-2026-y.

[15] A. Zulkifli, F.H. Tan, Z. Areeb, S.F. Stuart, J. Gomez, L. Paradiso, R.B. Luwor, Carfilzomib promotes the unfolded protein response and apoptosis in Cetuximab-resistant colorectal cancer, Int. J. Mol. Sci. 22 (13) (2021) 7114, https://doi.org/10.3390/ijms22137114.

[16] E.E. Manasanch, R.Z. Orlowski, Proteasome inhibitors in cancer therapy, Nat. Rev. Clin. Oncol. 14 (7) (2017) 417–433, https://doi.org/10.1038/nrclinonc.2016.206.

[17] E.G. Aird, M. Folkard, C.R. Mayes, P.J. Bownes, J.M. Lawson, M.C. Joiner, A purpose-built iodine-125 irradiation plaque for low dose rate low energy irradiation of cell lines *in vitro*, Br. J. Radiol. 74 (877) (2001) 56–61, https://doi.org/10.1259/bjr.74.877.740056.

[18] M.J. Seo, I.Y. Kim, D.M. Lee, Y.J. Park, M.Y. Cho, H.J. Jin, K.S. Choi, Dual inhibition of thioredoxin reductase and proteasome is required for auranofin-induced paraptosis in breast cancer cells, Cell Death. Dis. 14 (1) (2023) 42, https://doi.org/10.1038/s41419-023-05586-6.

[19] E.A. Prokhorova, A.Y. Egorshina, B. Zhivotovsky, G.S. Kopeina, The DNA-damage response and nuclear events as regulators of nonapoptotic forms of cell death, Oncogene 39 (1) (2020) 1–16, https://doi.org/10.1038/s41388-019-0980-6.

[20] L. Hu, H. Wang, Y. Zhao, J. Wang, (125)I seeds radiation induces paraptosis-like cell death via PI3K/AKT signaling pathway in HCT116 cells, Biomed. Res. Int. 2016 (2016) 8145495, https://doi.org/10.1155/2016/8145495.

[21] E. Kim, D.M. Lee, M.J. Seo, H.J. Lee, K.S. Choi, Intracellular Ca(2 +) imbalance critically contributes to paraptosis, Front. Cell Dev. Biol. 8 (2020) 607844, https://doi.org/10.3389/fcell.2020.607844.

[22] X. Jiang, B.R. Stockwell, M. Conrad, Ferroptosis: mechanisms, biology and role in disease, Nat. Rev. Mol. Cell Biol. 22 (4) (2021) 266–282, https://doi.org/10.1038/s41580-020-00324-8.

[23] N.G. Zaorsky, B.J. Davis, P.L. Nguyen, T.N. Showalter, P.J. Hoskin, Y. Yoshioka, G. C. Morton, E.M. Horwitz, The evolution of brachytherapy for prostate cancer, Nat. Rev. Urol. 14 (7) (2017) 415–439, https://doi.org/10.1038/nrurol.2017.76.

[24] C. Liu, L. Wang, H. Qiu, Q. Dong, Y. Feng, D. Li, C. Li, C. Fan, Combined strategy of radioactive (125)I seeds and salinomycin for enhanced glioma chemo-radiotherapy: evidences for ROS-mediated apoptosis and signaling crosstalk, Neurochem. Res. 43 (7) (2018) 1317–1327, https://doi.org/10.1007/s11064-018-2547-2.

[25] G.H. He, D.J. Xing, D. Jin, Y. Lu, L. Guo, Y.L. Li, D. Li, Scutellarin improves the radiosensitivity of non-small cell lung cancer cells to iodine-125 seeds via downregulating the AKT/mTOR pathway, Thorac. Cancer 12 (17) (2021) 2352–2359, https://doi.org/10.1111/1759-7714.14077.

[26] X. Yao, S. Lu, C. Feng, R. Suo, H. Li, Y. Zhang, Q. Chen, J. Lu, B. Wu, J. Guo, Tumor oxygenation nanoliposome synergistic hypoxia-inducible-factor-1 inhibitor enhanced Iodine-125 seed brachytherapy for esophageal cancer, Biomaterials 289 (2022) 121801, https://doi.org/10.1016/j.biomaterials.2022.121801.

[27] P.L. Vaddavalli, B. Schumacher, The p53 network: cellular and systemic DNA damage responses in cancer and aging, Trends. Genet. 38 (6) (2022) 598–612, https://doi.org/10.1016/j.tig.2022.02.010.

[28] X. Zhou, W. Zhang, M. Dou, Z. Li, Z. Liu, J. Li, C. Tian, Y. Yao, C. Wang, Y. Li, et al., (125)I seeds inhibit proliferation and promote apoptosis in cholangiocarcinoma cells by regulating the AGR2-mediated p38 MAPK pathway, Cancer Lett. 524 (2022) 29–41, https://doi.org/10.1016/j.canlet.2021.10.014.

[29] J.Y. Tang, F. Ou-Yang, M.F. Hou, H.W. Huang, H.R. Wang, K.T. Li, S. Fayyaz, C. W. Shu, H.W. Chang, Oxidative stress-modulating drugs have preferential anticancer effects - involving the regulation of apoptosis, DNA damage, endoplasmic reticulum stress, autophagy, metabolism, and migration, Semin. Cancer Biol 58 (2019) 109–117, https://doi.org/10.1016/j.semcancer.2018.08.010.

[30] M. Chaurasia, A.N. Bhatt, A. Das, B.S. Dwarakanath, K. Sharma, Radiation-induced autophagy: mechanisms and consequences, Free Radic. Res. 50 (3) (2016) 273–290, https://doi.org/10.3109/10715762.2015.1129534.

[31] S. Hanson, A. Dharan, V.J.P, S. Pal, B.G. Nair, R. Kar, N. Mishra, Paraptosis: a unique cell death mode for targeting cancer, Front. Pharmacol. 14 (2023) 1159409, https://doi.org/10.3389/fphar.2023.1159409.

[32] I.Y. Kim, M.J. Shim, D.M. Lee, A.R. Lee, M.A. Kim, M.J. Yoon, M.R. Kwon, H.I. Lee, M.J. Seo, Y.W. Choi, et al., Loperamide overcomes the resistance of colon cancer cells to bortezomib by inducing CHOP-mediated paraptosis-like cell death, Biochem. Pharmacol. 162 (2019) 41–54, https://doi.org/10.1016/j.bcp.2018.12.006.

[33] D. Senft, Z.A. Ronai, UPR, autophagy, and mitochondria crosstalk underlies the ER stress response, Trends Biochem. Sci. 40 (3) (2015) 141–148, https://doi.org/10.1016/j.tibs.2015.01.002.

[34] G. Lei, L. Zhuang, B. Gan, Targeting ferroptosis as a vulnerability in cancer, Nat. Rev. Cancer 22 (7) (2022) 381–396, https://doi.org/10.1038/s41568-022-00459-0.

[35] G. Lei, Y. Zhang, P. Koppula, X. Liu, J. Zhang, S.H. Lin, J.A. Ajani, Q. Xiao, Z. Liao, H. Wang, et al., The role of ferroptosis in ionizing radiation-induced cell death and tumor suppression, Cell Res. 30 (2) (2020) 146–162, https://doi.org/10.1038/s41422-019-0263-3.

[36] X. Lang, M.D. Green, W. Wang, J. Yu, J.E. Choi, L. Jiang, P. Liao, J. Zhou, Q. Zhang, A. Dow, et al., Radiotherapy and immunotherapy promote tumoral lipid oxidation and ferroptosis via synergistic repression of SLC7A11, Cancer Discov. 9 (12) (2019) 1673–1685, https://doi.org/10.1158/2159-8290.CD-19-0338.

[37] L.F. Ye, K.R. Chaudhary, F. Zandkarimi, A.D. Harken, C.J. Kinslow, P. S. Upadhyayula, A. Dovas, D.M. Higgins, H. Tan, Y. Zhang, et al., Radiation-induced lipid peroxidation triggers ferroptosis and synergizes with ferroptosis inducers, ACS Chem. Biol. 15 (2) (2020) 469–484, https://doi.org/10.1021/acschembio.9b00939.

[38] J. Su, C. Bian, Z. Zheng, H. Wang, L. Meng, Y. Xin, X. Jiang, Cooperation effects of radiation and ferroptosis on tumor suppression and radiation injury, Front. Cell Dev. Biol. 10 (2022) 951116, https://doi.org/10.3389/fcell.2022.951116.

[39] X. Chen, C. Yu, R. Kang, D. Tang, Iron metabolism in ferroptosis, Front. Cell Dev. Biol. 8 (2020) 590226, https://doi.org/10.3389/fcell.2020.590226.

[40] R. Wei, Y. Zhao, J. Wang, X. Yang, S. Li, Y. Wang, X. Yang, J. Fei, X. Hao, Y. Zhao, et al., Tagitinin C induces ferroptosis through PERK-Nrf2-HO-1 signaling pathway in colorectal cancer cells, Int. J. Biol. Sci. 17 (11) (2021) 2703–2717, https://doi.org/10.7150/ijbs.59404.

[41] T.B. Aydemir, R.J. Cousins, The multiple faces of the metal transporter ZIP14 (SLC39A14), J. Nutr. 148 (2) (2018) 174–184, https://doi.org/10.1093/jn/nxx041.
[42] Q. Zhou, Y. Meng, D. Li, L. Yao, J. Le, Y. Liu, Y. Sun, F. Zeng, X. Chen, G. Deng, Ferroptosis in cancer: from molecular mechanisms to therapeutic strategies, Signal. Transduct. Target. Ther. 9 (1) (2024) 55, https://doi.org/10.1038/s41392-024-01769-5.
[43] X. Liu, C. Yan, C. Chang, F. Meng, W. Shen, S. Wang, Y. Zhang, FOXA2 Suppression by TRIM36 exerts anti-tumor role in colorectal cancer via inducing NRF2/GPX4-regulated ferroptosis, Adv. Sci. 10 (35) (2023) e2304521, https://doi.org/10.1002/advs.202304521.
[44] X. Ma, X. Dong, Y. Xu, N. Ma, M. Wei, X. Xie, Y. Lu, W. Cao, G. Lu, W. Li, Identification of AP-1 as a critical regulator of glutathione peroxidase 4 (GPX4) transcriptional suppression and acinar cell ferroptosis in acute pancreatitis, Antioxidants. (Basel) 12 (1) (2022) 100, https://doi.org/10.3390/antiox12010100.
[45] W. Pan, L. Xiang, X. Liang, W. Du, J. Zhao, S. Zhang, X. Zhou, L. Geng, S. Gong, W. Xu, Vitronectin destroyed intestinal epithelial cell differentiation through activation of PDE4-mediated ferroptosis in inflammatory bowel disease, Mediators. Inflamm. 2023 (2023) 6623329, https://doi.org/10.1155/2023/6623329.
[46] Y. Zhang, J. Zhang, D. Feng, H. Zhou, Z. Gui, M. Zheng, Z. Hang, Z. Wang, Z. Wang, M. Gu, et al., IRF1/ZNF350/GPX4-mediated ferroptosis of renal tubular epithelial cells promote chronic renal allograft interstitial fibrosis, Free Radic, Biol. Med. 193 (Pt 2) (2022) 579–594, https://doi.org/10.1016/j.freeradbiomed.2022.11.002.
[47] K. Hadian, B.R. Stockwell, The therapeutic potential of targeting regulated non-apoptotic cell death, Nat. Rev. Drug Discov. 22 (9) (2023) 723–742, https://doi.org/10.1038/s41573-023-00749-8.